

An Ordered Water Channel in *Staphylococcus aureus* FabI: Unraveling the Mechanism of Substrate Recognition and Reduction

Johannes Schiebel,^{1,2,‡} Andrew Chang,³ Benjamin Merget,¹ Gopal R. Bommineni,³ Weixuan Yu,³
Lauren A. Spagnuolo,³ Michael V. Baxter,³ Mona Tareilus,² Peter J. Tonge,^{3,*} Caroline Kisker,^{2,*}
Christoph A. Sotriffer^{1,*}

¹Institute of Pharmacy and Food Chemistry, University of Wuerzburg, Am Hubland, D-97074
Wuerzburg, Germany

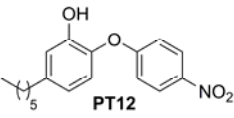
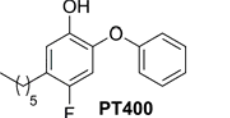
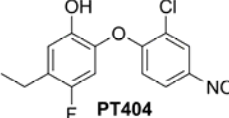
²Rudolf Virchow Center for Experimental Biomedicine, Institute for Structural Biology,
University of Würzburg, Josef-Schneider-Str. 2, D-97080 Würzburg, Germany

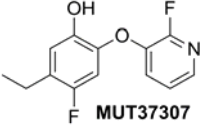
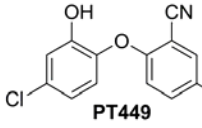
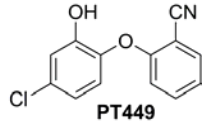
³Institute for Chemical Biology & Drug Discovery, Department of Chemistry, Stony Brook
University, Stony Brook, New York 11794-3400, USA

[‡]Present address: Department of Pharmaceutical Chemistry, University of Marburg, Marbacher
Weg 6, D-35032 Marburg, Germany

Supplemental Tables

Table S1. Data Collection and Refinement Statistics

	saFabI-NADP ⁺ -PT12	saFabI-NADP ⁺ -PT400	saFabI-NADP ⁺ -PT404
Inhibitor			
Crystallization			
Protein concentration (mg/ml)	15.0	15.0	15.0
Crystallization condition	0.1 M K/Na-phosphate pH 6.5 47% MPD	0.1 M K/Na-phosphate pH 6.5 39% MPD	0.1 M K/Na-phosphate pH 6.5 47% MPD
Cryoprotectant	none	none	none
Data collection			
Cell dimensions			
a, b, c (Å)	89.4, 94.8, 94.8	90.4, 94.9, 94.9	89.2, 94.9, 94.9
α, β, γ (°)	98.3, 111.4, 97.5	98.2, 97.2, 112.5	98.5, 111.5, 97.3
Space group	P1	P1	P1
Resolution ^a (Å)	40.8-2.30 (2.42-2.30)	38.6-2.02 (2.13-2.02)	40.7-2.15 (2.27-2.15)
Observed reflections	266,684 (38,821)	360,497 (52,058)	327,098 (47,457)
Unique reflections	120,978 (17,617)	181,260 (26,181)	148,864 (21,614)
Completeness (%)	96.8 (96.1)	97.8 (97.0)	97.5 (96.7)
Average redundancy	2.2 (2.2)	2.0 (2.0)	2.2 (2.2)
R _{merge} ^b (%)	10.7 (43.5)	5.7 (37.6)	11.0 (41.7)
R _{pim} ^c (%)	9.6 (39.1)	5.7 (37.6)	9.8 (37.4)
<I / σ(I)>	6.1 (2.0)	7.5 (2.0)	6.0 (2.1)
Monomers per AU	8	8	8
Refinement			
Resolution (Å)	40.8-2.30	38.4-2.02	40.7-2.15
R _{cryst} ^d (%)	15.2	14.5	17.0
R _{free} (%)	21.3	18.5	23.0
Number of atoms	17,717	18,217	18,382
rmsd bond lengths (Å)	0.010	0.013	0.012
rmsd bond angles (°)	1.68	1.78	1.74
Average B-factor (Å ²)	38.7	33.5	23.3
Ramachandran-plot ^e			
Favored (%)	95.7	96.6	96.3
Allowed (%)	4.1	3.4	3.4
Outliers (%)	0.2	0.0	0.3
Maximum likelihood based estimated coordinate error (Å)	0.15	0.10	0.13
PDB code	4D41	4D42	4D43

	saFabI-NADP ⁺ -MUT37307	saFabI-NADP ⁺ -PT449	ecFabI-NAD ⁺ -PT449
Inhibitor	 MUT37307	 PT449	 PT449
Crystallization			
Protein concentration (mg/ml)	15.0	19.0	13.0
Crystallization condition	0.1 M K/Na-phosphate pH 6.5 41% MPD	0.1 M K/Na-phosphate pH 6.5 47% MPD	0.08 M NH ₄ Ac 0.1 M CAPS pH 10.5 20% PEG 3350
Cryoprotectant	none	none	20% ethylene glycol
Data collection			
Cell dimensions			
a, b, c (Å)	90.0, 94.7, 94.8	90.1, 95.2, 95.2	79.1, 79.1, 322.3
α, β, γ (°)	98.1, 97.4, 112.2	98.4, 97.5, 111.5	90, 90, 120
Space group	P1	P1	P6 ₁ 22
Resolution ^a (Å)	33.6-1.80 (1.90-1.80)	46.6-2.15 (2.27-2.15)	47.0-2.00 (2.11-2.00)
Observed reflections	1,011,220 (146,182)	543,061 (80,880)	794,472 (114,237)
Unique reflections	254,237 (36,744)	152,227 (22,139)	41,818 (5,947)
Completeness (%)	97.5 (96.4)	98.2 (97.6)	100.0 (100.0)
Average redundancy	4.0 (4.0)	3.6 (3.7)	19.0 (19.2)
R _{merge} ^b (%)	7.1 (61.7)	9.7 (56.0)	13.7 (124.6)
R _{pim} ^c (%)	4.1 (35.7)	6.1 (34.1)	3.2 (29.0)
<I / σ(I)>	11.4 (2.3)	8.3 (2.2)	16.2 (2.4)
Monomers per AU	8	8	2
Refinement			
Resolution (Å)	33.6-1.80	46.6-2.15	68.5-2.00
R _{cryst} ^d (%)	14.0	17.4	16.6
R _{free} (%)	17.0	22.7	20.6
Number of atoms	18,237	17,357	3,996
rmsd bond lengths (Å)	0.015	0.012	0.015
rmsd bond angles (°)	1.87	1.68	1.75
Average B-factor (Å ²)	28.8	36.8	41.6
Ramachandran-plot ^e			
Favored (%)	97.2	96.6	97.3
Allowed (%)	2.8	3.4	2.7
Outliers (%)	0.0	0.0	0.0
Maximum likelihood based estimated coordinate error (Å)	0.06	0.14	0.10
PDB code	4D44	4D45	4D46

^a Values in parenthesis refer to the highest resolution shell

$$^b R_{merge} = \frac{\sum_{hkl} \sum_i |I_i - \langle I \rangle|}{\sum_{hkl} \sum_i I_i}$$

$$^c R_{pim} = \frac{\sum_{hkl} [1/(N-1)]^{1/2} \sum_i |I_i - \langle I \rangle|}{\sum_{hkl} \sum_i I_i} \quad ^1$$

$$^d R_{cryst} = \frac{\sum_{hkl} |F_{obs} - F_{calc}|}{\sum_{hkl} F_{obs}}$$

^e According to Molprobability ²

Table S2. Nucleotide primers for site-directed mutagenesis

Name	Primer sequence
D249A forward	5' CAGGTGAAAATATTCATGTAGCGAGCGGATTCCACGCAATTAA 3'
D249A reverse	5' TTAATTGCGTGGAATCCGCTCGCTACATGAATATTTTCACCTG 3'
S189A forward	5' CGCGTTAATGCAATTGCGGCTAGTCCAATCCG 3'
S189A reverse	5' CGGATTGGACTAGCCGCAATTGCATTAACGCG 3'
Y147F forward	5' GCATTGTTGCAACAACATTTTTAGGTGGCGAATTCGC 3'
Y147F reverse	5' GCGAATTCGCCACCTAAAAATGTTGTTGCAACAATGC 3'

Table S3. Simulation averages of the rmsd values for the five wild-type saFabI MD simulations with respect to the saFabI-NADP⁺-PT400 starting structure [Å]

rmsd (vs. X-ray)	saFabI ₂		saFabI ₄		saFabI ₄ -NADP ⁺		saFabI-NADP ⁺ -PT400		saFabI ₄ -NADP ⁺ -PT400	
	all atoms	C _α atoms	all atoms	C _α atoms	all atoms	C _α atoms	all atoms	C _α atoms	all atoms	C _α atoms
all protein residues	2.55 ± 0.32	1.97 ± 0.31	2.15 ± 0.22	1.61 ± 0.18	1.74 ± 0.18	1.26 ± 0.15	1.87 ± 0.15	1.25 ± 0.14	1.72 ± 0.15	1.25 ± 0.12
less flexible residues ^a	1.71 ± 0.16	1.18 ± 0.13	1.62 ± 0.15	1.19 ± 0.11	1.46 ± 0.13	1.05 ± 0.09	1.60 ± 0.12	1.04 ± 0.08	1.44 ± 0.11	1.01 ± 0.08
flexible residues ^b	4.52 ± 0.67	3.78 ± 0.70	3.52 ± 0.42	2.71 ± 0.39	2.50 ± 0.35	1.85 ± 0.33	2.70 ± 0.34	1.91 ± 0.36	2.52 ± 0.27	1.94 ± 0.25
β-strands ^c	1.01 ± 0.11	0.69 ± 0.10	1.41 ± 0.15	1.09 ± 0.13	1.13 ± 0.13	0.85 ± 0.10	0.79 ± 0.08	0.46 ± 0.05	1.12 ± 0.11	0.85 ± 0.10

^a the most flexible regions (residues 3-7, 40-47, 99-113, 152-156 and 194-210) were omitted during fitting and rmsd calculation

^b rmsd for the most flexible regions with fitting according to ^a

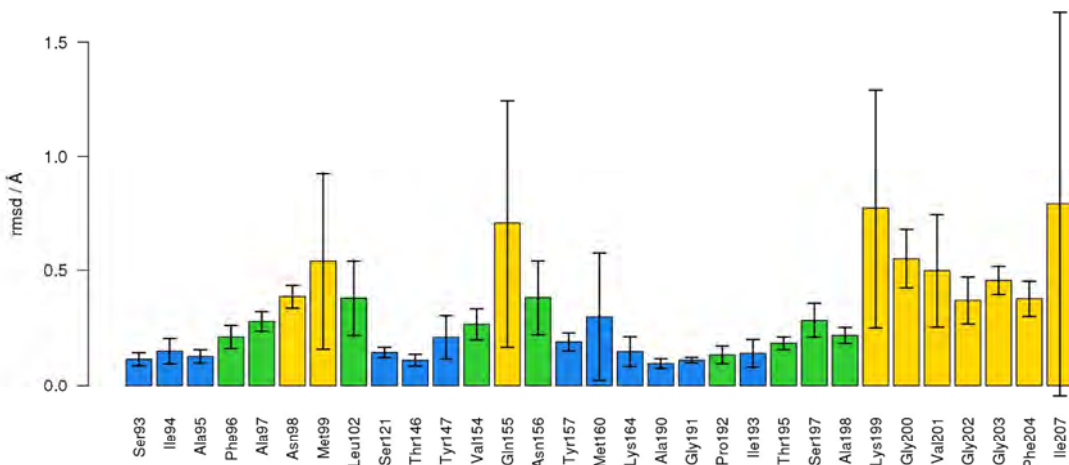
^c rmsd for β-strand residues only (37 residues)

Table S4. Simulation averages of the rmsd values for the tetrameric wild-type and mutant saFabI MD simulations (saFabI₄-NADP⁺-PT400) with respect to the saFabI-NADP⁺-PT400 starting structure [Å]

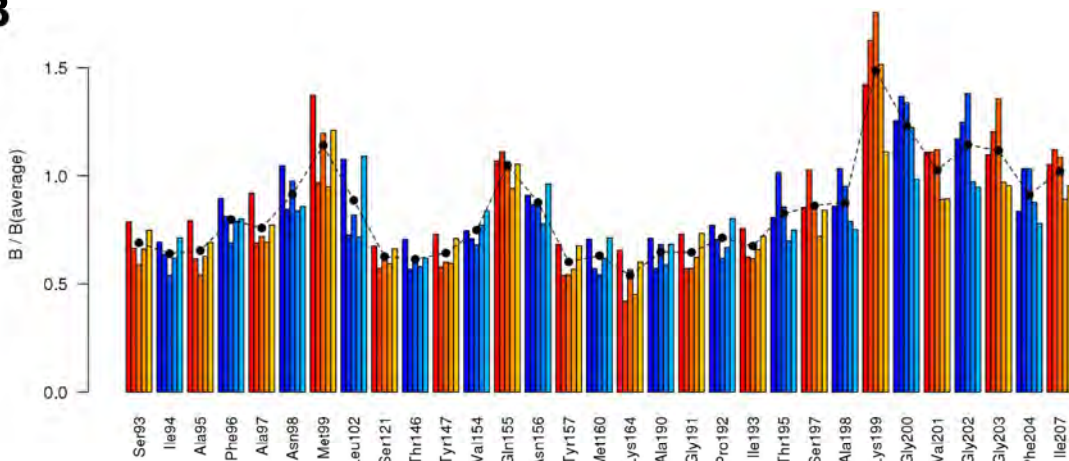
rmsd (vs. X-ray)	D249A	Y147F	S189A	wild-type
C _α atoms of all residues	1.29 ± 0.17	1.14 ± 0.09	1.27 ± 0.13	1.25 ± 0.12

Supplemental Figures

A



B



C

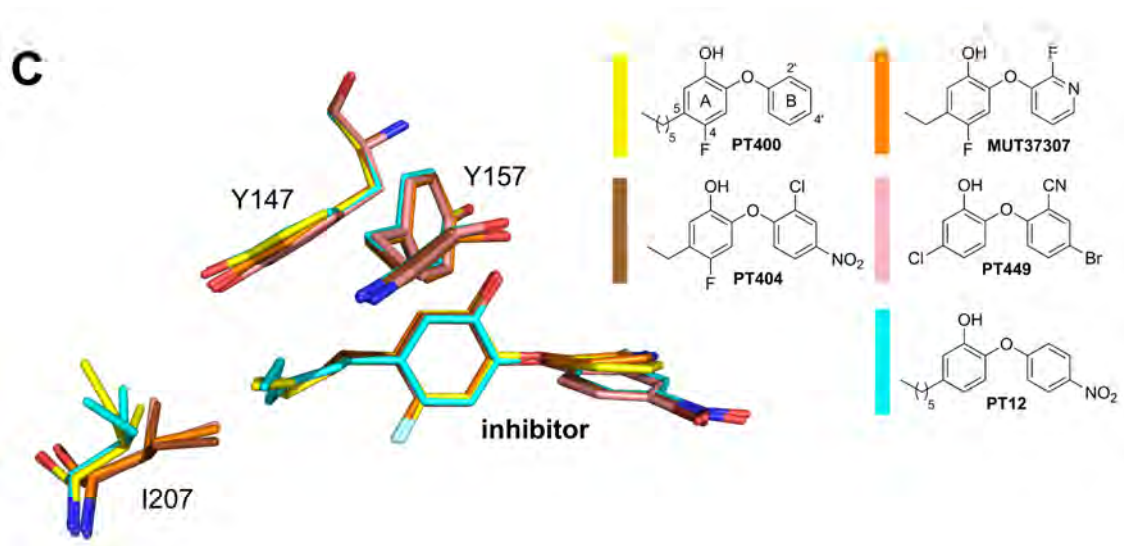


Figure S1. Comparison of saFabI structures in the presence of different inhibitors. (A) Per-residue rmsd values for the binding-site residues. The superposition of the five saFabI-inhibitor structures (one subunit per structure (chain A), all-atom fit) and the calculation of per-atom rmsd values were performed using theseus³ in order to evaluate the structural influence of inhibitor binding. The resulting barplot was then generated with R (for explanation of the color code, see below). The depicted per-residue rmsd values were calculated as the mean of all per-atom rmsd values of an individual binding-site residue. The corresponding standard deviations indicate the variability of conformational differences within a particular residue (e.g. the main chain atoms of Ile207 are relatively conserved among the 5 structures, whereas the side chain atoms differ more drastically in their conformation leading to a high per-atom rmsd standard deviation for this residue; see also panel C). (B) Mobility of the binding-site residues. Per-residue B-factors were calculated for each of the five saFabI-inhibitor structures using the program Baverage from the CCP4 suite⁴ and divided by the average B-factor of the respective structure. The depicted graph was generated using R and shows the normalized B-factor for all binding-site residues (alternating in color from red to blue) of each structure. For a specific residue, the bars are sorted by structure with decreasing color intensity (from left to right: PT12, PT400, PT404, MUT37307 and PT449) with the mean value represented by the black filled circle. Using these mean values, a classification in rigid, medium flexible and very flexible residues was performed by choosing values of 0.7 and 0.9 as cutoffs. In panel A these three classes of residues are represented by the colors blue, green and yellow, respectively. (C) Structural influence of inhibitor binding to saFabI. The inhibitors and selected binding-site residues are shown for the structures superimposed as described in panel A. The color code is defined in the legend.

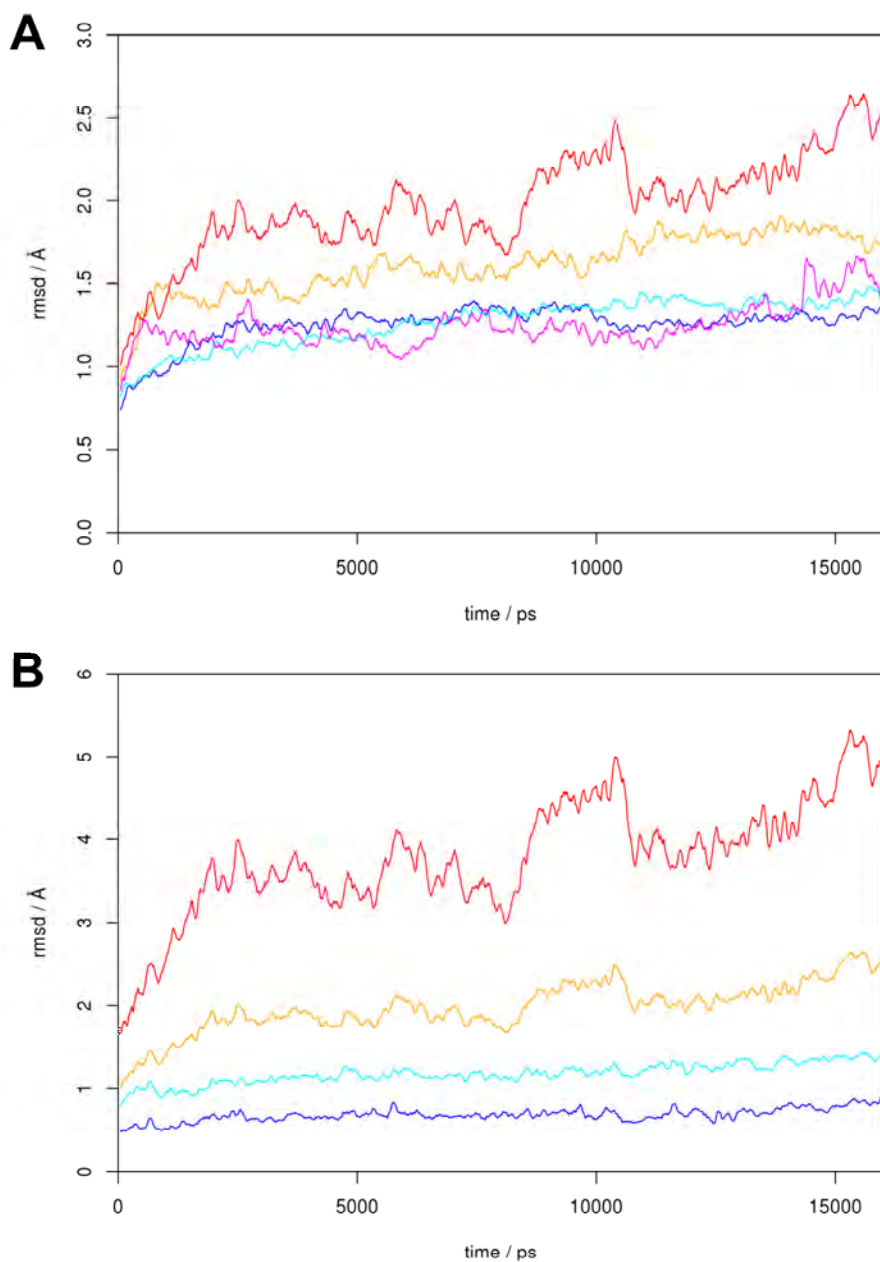


Figure S2. Trajectory rmsd values. (A) Rmsd values for the five wild-type MD simulations (saFabI₄-NADP⁺-PT400, blue; saFabI₁-NADP⁺-PT400, magenta; saFabI₄-NADP⁺, cyan; saFabI₄, orange; saFabI₂, red). Calculations were performed using all protein C_α-atoms. (B) Rmsd values for selected atoms of the saFabI₂ simulation. Calculations were performed using all protein C_α-atoms (orange, 254 atoms per monomer), all C_α-atoms excluding the most flexible residues (see below) (cyan, 204 atoms per monomer) or the C_α-atoms of β-strand residues only (blue, 37 atoms per monomer). In addition, rmsd values for the most flexible saFabI residues (3-7, 40-47, 99-113, 152-156 and 194-210) were calculated based on a fitting procedure using all C_α-atoms excluding those residues (red, 50 atoms per monomer), which allows an evaluation of the conformational

variability of these protein regions. Both plots were generated using R and averaging over 100 ps
5.

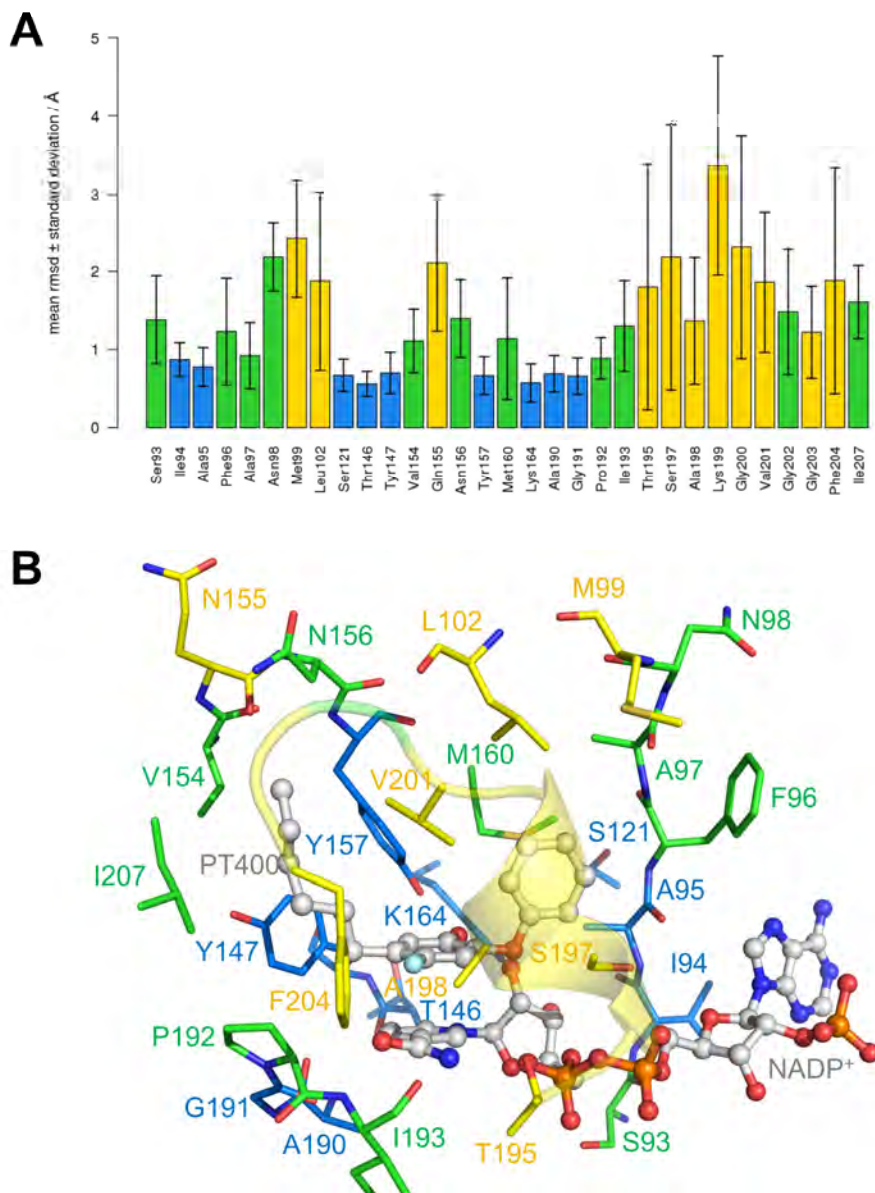


Figure S3. SaFabI binding pocket mobility. (A) Per-residue rmsd values for the binding-site residues. The calculation of the rmsd values was based on an all-atom fit of all residues for the saFabI₄-NADP⁺-PT400 MD snapshots. Conformational variability is indicated by the rmsd values, whereas the flexibility of the individual residues is represented by the corresponding standard deviations. This graph was generated using R. Overall, the same trend was observed by a comparison of the saFabI structures from this study and the analysis of the associated B-factors (cf. Figure S1). (B) Binding-site residue classification by flexibility. This classification is based on per-residue root mean square fluctuations (rmsf). Rigid, medium flexible and the most flexible residues are depicted as blue, green and yellow sticks, respectively (the same color code was also used for panel A). To enable a classification in three similarly sized groups, 0.6 and 1.0 Å rmsf-

cutoffs were chosen. The SBL is shown in transparent cartoon representation and the cofactor and inhibitor as ball-and-stick model.

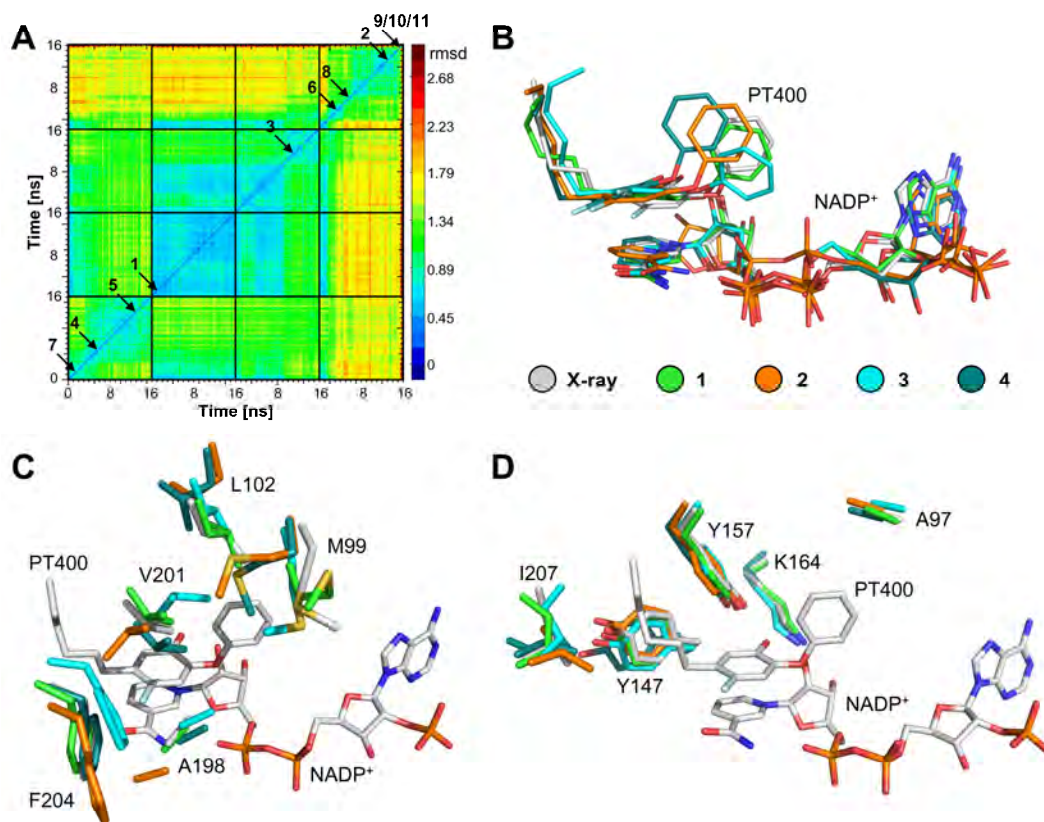


Figure S4. Hierarchical clustering analysis. (A) Combined 2D-rmsd plot for the C_α-atoms of the 31 binding-site residues of the four monomers within the saFabI₄-NADP⁺-PT400 MD simulation. The binding pockets of monomers 1 to 4 are represented by the black-framed squares. Calculation of rmsd values was performed in 100 ps intervals. Black arrows indicate the chosen cluster representatives (numbered consecutively according to cluster size; cluster 1 accounts for 44% of all snapshots, 2 = 13.7%, 3 = 11.1%, 4 = 9.7%, 5 = 9.6%, 6 = 4.1%, 7 = 3.5%, 8 = 2.7%, 9 = 0.6%, 10 = 0.5%, 11 = 0.4%). (B) Representative inhibitor and cofactor geometries. The binding modes of PT400 and NADP⁺ are shown for clusters 1-4 (colored according to the legend). The ligands of the saFabI-NADP⁺-PT400 crystal structure are shown as a reference in gray. (C) Conformations of selected flexible binding-site residues for the first four cluster representatives. (D) Conformations of selected rigid binding-site residues for the first four cluster representatives.

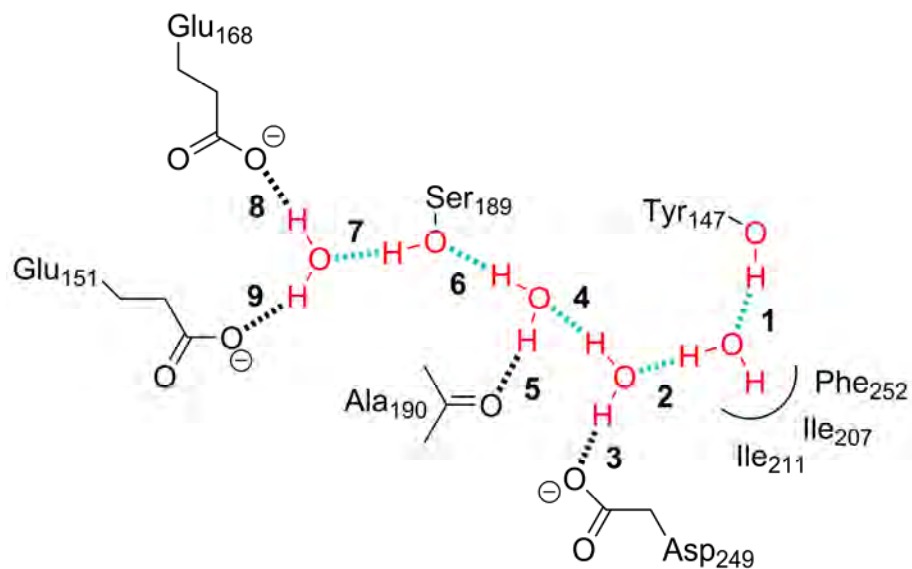


Figure S5. Schematic representation of the water-network connecting Tyr147 with the interior of the saFabI homo-tetramer. Simulation-averaged distances and occupancies of the hydrogen bonding interactions in the saFabI₄-NADP⁺-PT400 MD simulation (monomer 2) are given as: $2.8 \pm 0.1 \text{ \AA}$, 76% (1); $2.8 \pm 0.1 \text{ \AA}$, 69% (2); $2.7 \pm 0.1 \text{ \AA}$, 80% (3); $2.8 \pm 0.1 \text{ \AA}$, 88% (4); $2.8 \pm 0.1 \text{ \AA}$, 55% (5); $2.8 \pm 0.1 \text{ \AA}$, 76% (6); $2.7 \pm 0.1 \text{ \AA}$, 96% (7); $2.7 \pm 0.1 \text{ \AA}$, 95% (8); $2.7 \pm 0.1 \text{ \AA}$, 96% (9).

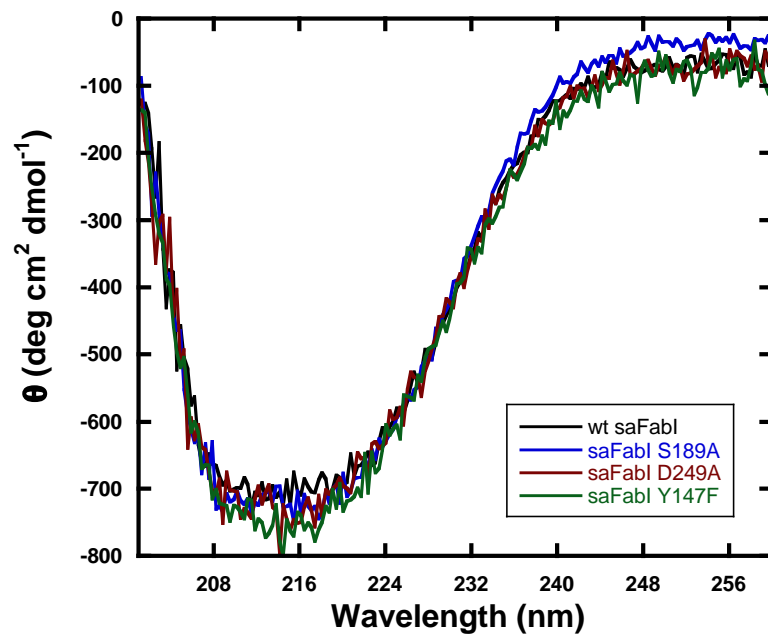


Figure S6. CD spectra showing a similar folding pattern for the water channel variants compared to the wild-type saFabI enzyme.

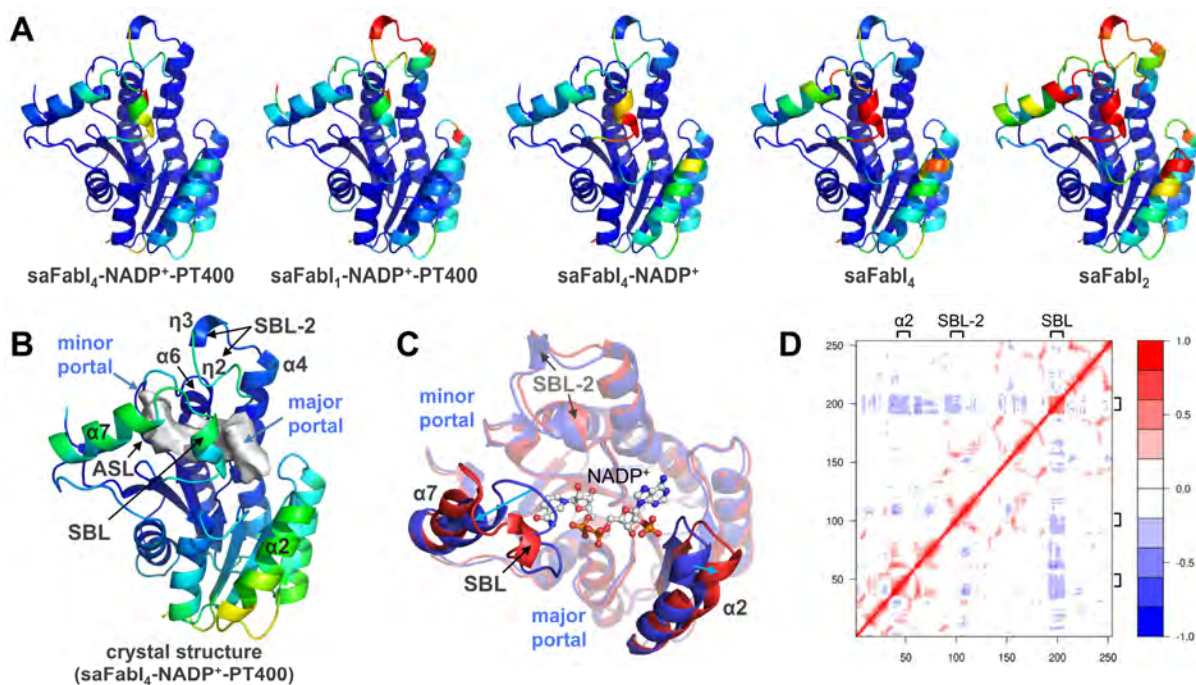


Figure S7. Conformational variability of saFabI. (A) Visualization of the B-factors for the five wild-type MD simulations. B-factors were averaged over the four monomers and plotted on monomer 3 of the saFabI-NADP⁺-PT400 structure. Colors indicate the B-factor value of each residue (blue to red = 5 to 85 Å²). (B) Visualization of the B-factor for the saFabI-NADP⁺-PT400 crystal structure. B-factors were averaged over the four monomers and plotted on monomer 3 of the structure. Colors indicate the B-factor value of each residue (blue to red = 20 to 85 Å²). (C) Essential dynamics of saFabI (calculated with ptraj and IED⁶). The first (blue) and last (red) frames along the principal mode of the 16 ns saFabI₂ MD trajectory are shown for one monomer exemplarily. Blue arrows indicate the anti-correlated movement of the SBL and helix $\alpha 2$. NADP⁺ of the saFabI-NADP⁺-PT400 structure is shown as reference (colored ball-and-stick model). See also Movie S1. (D) Dynamic cross-correlation map (shown for the same monomer of the saFabI₂ MD simulation). This graph was generated using the statistical framework R.

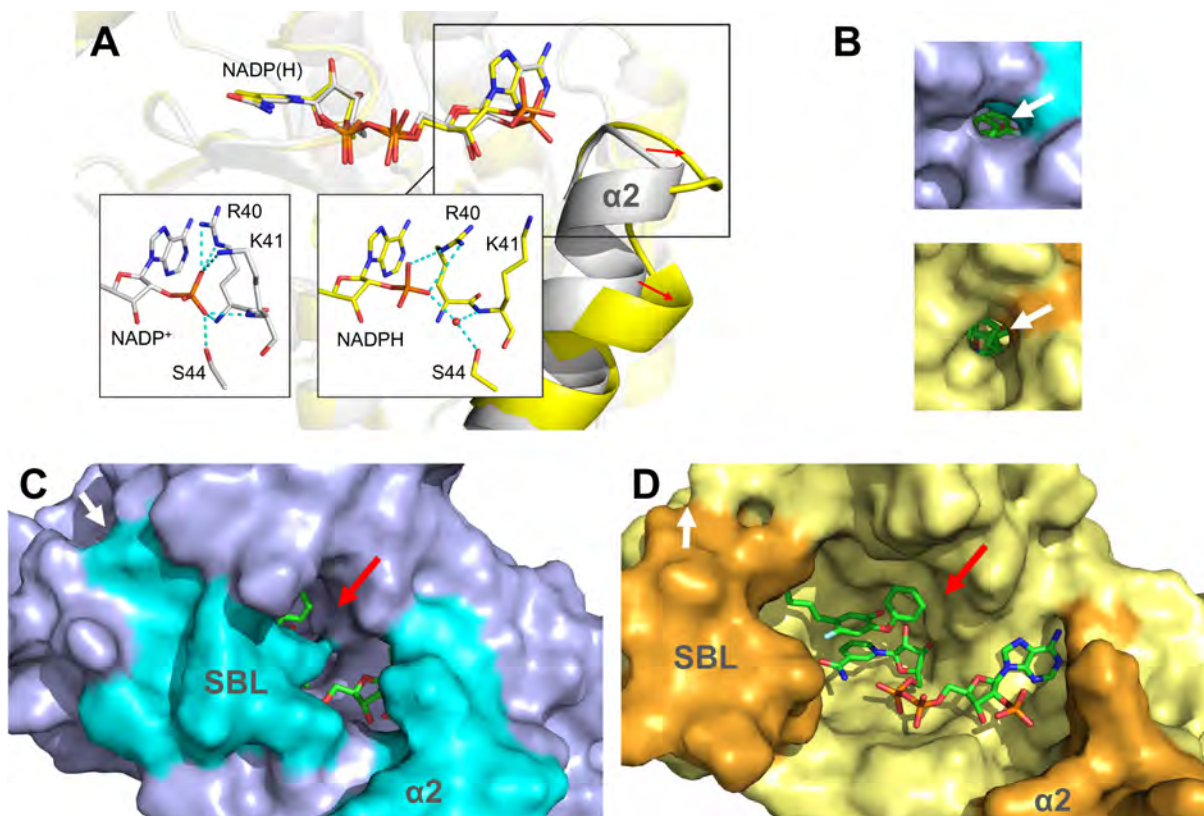


Figure S8. Cofactor and substrate binding process. (A) Conformational variability of the saFabI helix $\alpha 2$. The conformations of helix $\alpha 2$ as well as the interactions with the NADP(H) 2'-phosphate⁷ differ between the saFabI-NADP⁺-PT400 (gray) and saFabI-NADPH-CG400549 (yellow; PDB-code: 4CV1) structures. Red arrows indicate the shift of helix $\alpha 2$ in the CG400549-bound structure. (B) Minor portal states. The minor portals of the structures shown also in panels C and D are depicted using the same color code and scale. (C) Closed state of the major portal. Red and white arrows indicate the location of the major and minor portal, respectively. The saFabI-NADP⁺-PT400 crystal structure is shown in blue surface representation with the SBL and helix $\alpha 2$ indicated in cyan (including hydrogens added using tleap). PT400 and NADP⁺ are shown as green sticks. (D) Opened state of the major portal. The structural representative of a hierarchical clustering analysis of the saFabI₂ MD trajectory with the most opened major portal ($t = 14.7$ ns, same monomer as in Figure S7C-D and Movie S1) is shown in yellow surface representation with the SBL and helix $\alpha 2$ highlighted in orange. The same scale and view was used as for panel C. PT400 and NADP⁺ are shown as reference in green.

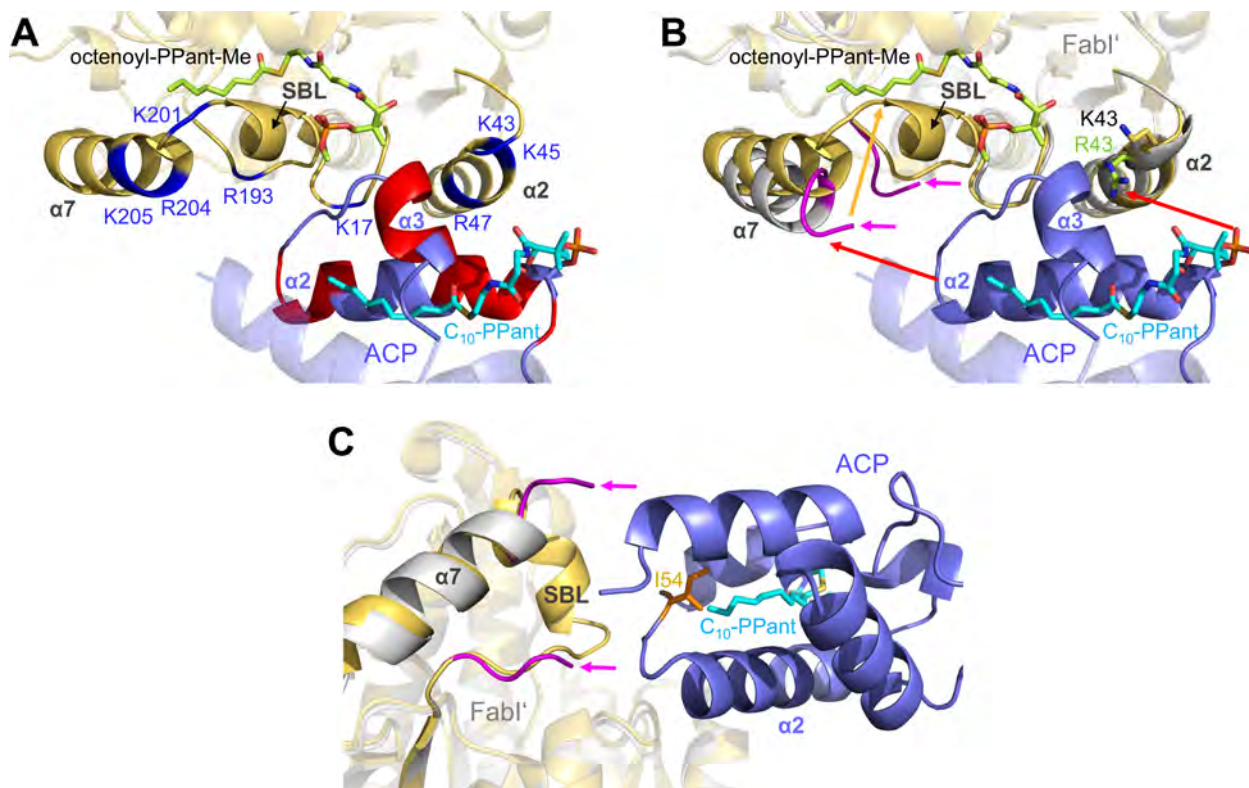


Figure S9. The ecFabI-ACP encounter complex. To derive a full ACP model, decanoyl-ecACP (lilac, PDB-code: 2FAE) was superimposed onto the partial ACP model of the 2FHS-structure (for details see Figure 6). (A) ACP binds close to the major portal. According to the new interpretation of the 2FHS model, the conserved acidic ACP patches (depicted in red) interact with basic FabI regions mainly located on helices $\alpha 2$, $\alpha 7$ and the SBL (indicated in blue; PDB-code: 1QSG). The putative binding mode for the substrate analog *trans*-2-octenoyl-PPant-Me was generated via docking and is depicted in green. The decanoyl-substrate (C_{10} -PPant) of the original ACP model (lilac, PDB-code: 2FAE) is depicted in cyan. (B) Putative ACP binding process. Red and golden arrows indicate the proposed movements of ACP and the SBL upon substrate injection, respectively. The disordered SBL of the 2FHS-structure is highlighted in magenta. The 1QSG ecFabI-NAD⁺-triclosan structure (golden) displays a closed SBL and was superimposed onto the FabI monomer of the new model (gray) as a reference (also depicted in panels A and C). (C) Proposed substrate delivery. Our new ecFabI-ACP complex model is shown in lilac (ACP) and gray (FabI) with the disordered SBL highlighted in magenta. In contrast, the SBL is in the closed state for the 1QSG ecFabI-NAD⁺-triclosan structure (golden). The ACP residue Ile54 (orange) is located in the FabI-ACP interface and likely contributes to the binding

of the substrate inside the ACP-fold. The decanoyl-substrate of the 2FAE-structure, C₁₀-PPant, is depicted in cyan.

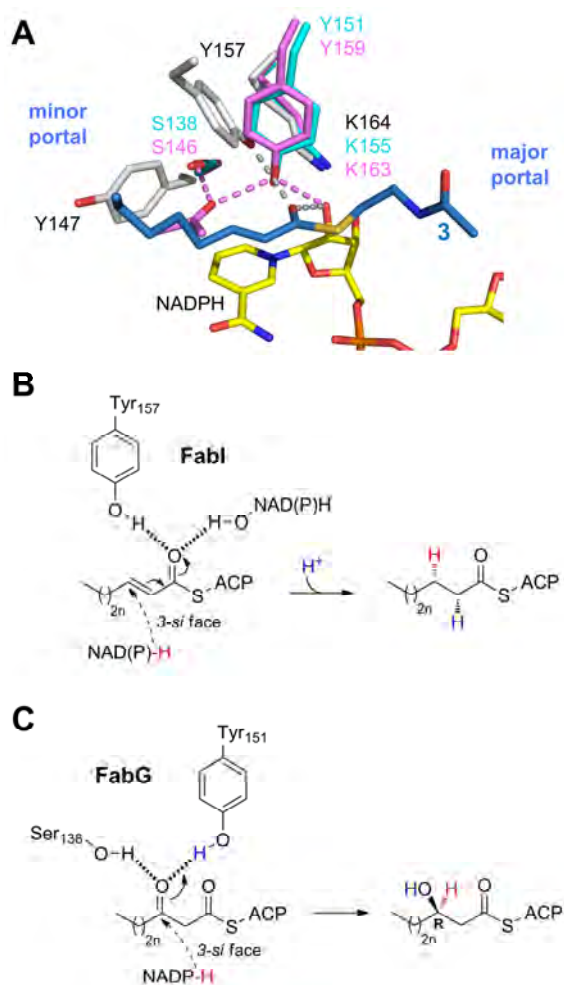
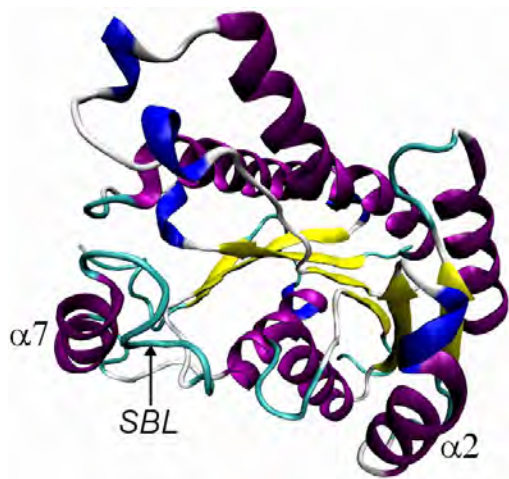


Figure S10. Comparison of substrate binding to FabI and FabG. (A) Superposition of saFabI (gray; saFabI-NADP⁺-PT400 structure), FabG (cyan; PDB-code: 1Q7B) and 7 α -hydroxysteroid dehydrogenase (HSDH) (pink; PDB-code: 1FMC). The proposed substrate binding modes (for HSDH, the carbonyl group of the reaction product 7-oxo glycochenodeoxycholic acid is shown), hydrogen bonding networks and catalytic triad residues are depicted. In contrast to FabI, the negative charge formed by the hydride transfer is developing on the β -keto group in the case of the related FabG protein⁸. Since the β -carbon of the FabG β -ketoacyl-ACP substrate should be similarly positioned with respect to the reactive *pro*-4S hydride as the FabI enoyl-ACP substrate C3 carbon, one would expect that the oxyanion hole has to be shifted two carbon atoms towards the minor portal in the case of FabG. Indeed, as for the classical SDR protein 7 α -hydroxysteroid dehydrogenase (HSDH)⁹, the oxyanion hole is created directly above the reactive NADPH hydride. This is achieved by a substitution of Tyr147 by a serine and the exchange of the YX₆K-motif in FabI to YX₃K in FabG⁸. (B, C) Substrate binding to FabI and FabG, respectively. The

geometrically different oxyanion holes of FabI and FabG likely bind the thioester carbonyl and β -keto oxygens, respectively.

Supplemental Movies



Movie S1. Essential dynamics of saFabI (calculated with ptraj and IED⁶). The dynamics along the principal mode of the 16 ns saFabI₂ MD trajectory are shown for one monomer exemplarily (colored according to its secondary structure). The view is similar to that depicted in Figure S7C. Please note the widening of the central binding cavity located on top of the β -sheet (yellow) via the anti-correlated movements of helix $\alpha 2$ and the SBL (labeled in the still frame during the first four seconds of the movie). This movie was produced using VMD and has been smoothed (trajectory smoothing window size = 10 frames).

Supplemental Experimental Procedures

Circular Dichroism

Prior to analysis, saFabI was dialyzed in low salt buffer (10 mM potassium phosphate pH 7.5, 100 mM KCl) to a concentration of 5-10 μ M. Circular dichroism (CD) was performed using a Chirascan CD spectrophotometer (Applied Photophysics) at 20°C. The cells had a path length of 1 cm, and spectra were recorded from 260 to 200 nm for far-UV.

Supplemental Results

Molecular Dynamics Simulations

We initiated eight saFabI MD simulations for mainly three reasons: (1) To learn more about the dynamics involved in the inhibition of saFabI (saFabI₄-NADP⁺-PT400 and saFabI₁-NADP⁺-PT400 simulations), (2) to explore the process of cofactor and substrate binding as well as product release (saFabI₄-NADP⁺, saFabI₄ and saFabI₂ simulations), and (3) to investigate the catalytic mechanism of this important drug target (all wild-type and mutant simulations). The MD trajectories of saFabI excluding cofactor and PT400 displayed larger conformational variability and mobility as highlighted by the simulation-averaged rmsd values and standard deviations, respectively (Table S3). In particular the apo-simulations were characterized by a rising rmsd over time indicating a directional movement as described in the main text (Figures S2A and S7). However, when omitting the most flexible regions participating in these motions during the calculation of the rmsd values, this effect was diminished (Table S3, Figure S2B).

To gain insights into the motions characterizing the binding-site, we analyzed the dynamic behavior of the corresponding amino acids. Although we only explicitly discuss the dynamic profile of the binding-site residues for the saFabI₄-NADP⁺-PT400 simulation, similar observations were made for all trajectories. As expected, the SBL residues (amino acids 194-204) sealing the binding site displayed the largest conformational diversity and mobility as revealed by an analysis of the per-residue rms deviations and fluctuations (Figure S3; this is confirmed by a B-factor analysis of the saFabI structures from this study depicted in Figure S1B). Interestingly, Leu102, which was found to be present in an alternative, more opened state in our diphenyl ether-bound saFabI structures, also showed enhanced fluctuations. Moreover, Met99 is characterized by an increased conformational variability and mobility. This residue was shown to be involved in conferring selectivity to two clinical trial inhibitors towards the saFabI homologue¹⁰ and, thus, its flexibility might change upon binding of such compounds contacting Ala97. Importantly, most residues surrounding the reactive site of the cofactor including the catalytic triad residues (amino acids 190-193, 146-147, 157 and 164) were found to be rather rigid, facilitating the precise relative orientation of substrate and cofactor and, thus, enabling the proceeding of the catalyzed reaction from a stereoelectronic perspective. In fact, Bell et al. found that the presence of the InhA residue Phe149 (corresponding to Tyr147 in saFabI) is important for the correct positioning

of the *pro*-4S hydride in a pseudoaxial orientation competent for catalysis¹¹. In addition to these residues surrounding the nicotinamide ring of the cofactor, the amino acid stretch including residues 93-97 displays relatively low rmsd values and standard deviations and might, thus, act as a platform for the binding of the PPant moiety of the substrate.

These trends were confirmed by a hierarchical clustering analysis based on the 2D-rmsd values for all four subunits of the saFabI₄-NADP⁺-PT400 simulation (Figure S4A). Whereas monomers 1-3 displayed relatively homogenous binding-site snapshots, monomer 4 was characterized by increased heterogeneity and, thus, accounted for over 50% of all cluster representatives. A detailed analysis of the dynamics sampled by this monomer revealed that the anti-correlated opening of the binding-site (Figure S7C) partially occurs for this subunit (data not shown). The MD trajectory for this monomer might, thus, represent the start of an inhibitor dissociation process. Interestingly, the electron density of the starting crystal structure was less well defined for this monomer compared to all other subunits. Hence, subtle structural perturbations might have led to the observation of an initiated PT400 dissociation process in the MD trajectory for this monomer. Figure S4 shows selected residues of the structural representatives for the four largest clusters of the hierarchical clustering analysis (numbered consecutively from 1 to 4) compared to the crystal structure. The enhanced conformational diversity of the PT400 B-ring described in the main text is clearly visible in Figure S4B. Moreover, the cluster representatives 2 and 4 reveal that Leu102 can indeed be present in a more opened state (Figure S4C). In contrast, the enhanced Met99 mobility is particularly due to extensive side chain motions. The catalytic triad residues, however, were found to be in a relatively conserved conformation for all clusters. In summary, the sampled conformations of the binding-site residues and in particular the cluster representatives may serve as an ideal starting point for the development of new saFabI inhibitors since induced-fit effects are highly dominant for saFabI^{7, 10, 12}.

Supplemental Discussion

Cofactor Binding Process

Given the limited size of both portals towards the closed saFabI binding pocket (Figures S8C and S8B, top), it is unclear how the much larger cofactor may actually enter this crevice. The anti-correlated opening of the SBL and helix $\alpha 2$ described in the main text may not only be important for substrate recognition but could additionally facilitate binding of NADPH (Figure S7C, Movie S1). Indeed, with respect to the closed character of the starting crystal structure that likely resembles a state close to the TS sampled during the hydride transfer of the reaction, the most opened structural representative of a hierarchical clustering analysis of the saFabI₂ MD snapshots displays a vastly enlarged major portal opening (Figure S8D), whereas the minor portal remains in its relatively closed state (Figure S8B, bottom). Our structures of saFabI in complex with the more substrate-like 2-pyridone inhibitors¹⁰ indeed are characterized by a more opened conformation of helix $\alpha 2$ compared to the diphenyl ether-bound structures (Figure S8A). Interestingly, the structural variation of helix $\alpha 2$ entails a change in the recognition pattern of the additional NADPH 2'-phosphate by the RKXXS-motif located at the N-terminus of this helix. The specificity for NADPH compared to the commonly used reducing agent NADH is unique for saFabI and closely related homologues⁷. An important question is, thus, whether the flexibility of helix $\alpha 2$ may contribute to NADPH specificity and cofactor binding. We assumed that the nature of the cofactor would not affect binding of the diphenyl ether. This was the basis for directly measuring residence times using the saFabI R40Q/K41N/S44L variant¹², which overlapped well with values measured via progress curve analysis in the wild-type enzyme. Moreover, the dissociation rate of PT52 ($k_{\text{off}} = 0.03 \text{ min}^{-1}$) from the E (wild-type)-NAD⁺-PT52 ternary complex is very similar to that from E (wild-type)-NADP⁺-PT52. Interestingly, the onset and degree of inhibition both increased in the presence of NADH/NAD⁺ relative to NADPH/NADP⁺. This is most likely attributed to a 2-fold slower rate of dissociation of NAD⁺ from the wild-type enzyme compared to NADP⁺. Consistently, the dissociation rate of NAD⁺ from *E. coli* FabI is estimated to be 4-fold slower than the dissociation of NADP⁺ from saFabI^{10, 12}. Thus, the higher binding affinity of NADPH/NADP⁺ to saFabI is mostly the result of a faster rate of association. The observed mobility of helix $\alpha 2$ explains why the selectivity for NADPH is based on an enhanced association rate. The additional negative charges of the NADPH 2'-phosphate may be attracted by

the more solvent-exposed RKXXS-motif taking advantage of the long-range character of electrostatic interactions (Figure S8A). Indeed, this phenomenon has been described as electrostatic steering and can particularly lead to an increase in on-rates^{13, 14}. However, bound NADP⁺ may be more quickly released from the wild-type saFabI enzyme compared to NAD⁺ due to the transient character of these interactions (Figure S8A) and since charge-assisted hydrogen bonds are not as favorable when exposed to bulk solvent¹⁵.

Substrate Recognition

All our results consistently indicate that the ACP substrate must be delivered to the FabI binding pocket via the major portal. This finally led to a new interpretation of the ecFabI-NAD⁺-DD-ACP structure (PDB code 2FHS, Figure 6), which places ACP adjacent to the major, and not the minor, portal. The new FabI-ACP model is further supported by the inspection of all structurally known ACP-protein complexes (PDB-entries 1F80, 2CG5, 2XZ0, 2XZ1, 3EJB, 3EJD, 3EJE, 3NY7, 4DXE, 4ETW, 4IHF, 4IHG, 4IHH, 4KEH). This analysis indicated that ACP helix α_{2ACP} , which includes Ser36 carrying the substrate at its N-terminus, is consistently involved in the protein-protein interface¹⁶ with frequent contributions from the N-terminal part of helix α_{3ACP} (for ACP secondary structure elements, we use the subscript ACP to clearly distinguish them from corresponding FabI elements). Since these helices contain three conserved acidic regions (including 2-4 acidic residues each; red ACP portions in Figure S9A), the interaction interface of the FAS-II enzymes is required to be electropositive¹⁶. FabI proteins harbor several basic residues surrounding the major portal, which are distributed over three secondary-structure elements - α_2 with 2-4 basic residues, the SBL including the attached N-terminus of helix α_7 with 1-4 basic residues and the loop containing residues 17-18 with up to two basic amino acids (Figure S9A). Whereas in the original FabI-ACP model only the N-terminus of helix α_{2ACP} was able to interact with FabI, the new model permits the interaction of the full helix α_{2ACP} and the N-terminus of α_{3ACP} with the basic FabI interface surrounding the major portal. Based on the original model, the ecFabI residues Lys201, Arg204 and Lys205 (part of helix α_7) were mutated to analyze the proposed interface¹⁷. However, all three residues are proposed to be involved in the interaction of FabI with the ACP molecule whether the substrate enters through either the minor or the major portal, and therefore the mutagenesis data support both the original and the new model.

We assume that the new FabI-ACP model is not in a catalytically competent state but rather constitutes the initial encounter complex prior to substrate injection. In line with this suggestion, the SBL was found to be disordered in the 2FHS-structure and no electron density was observed for the cofactor or substrate¹⁷. A comparison of the new FabI-ACP complex with our predicted substrate binding modes suggests that ACP has to move by approximately 12 Å (indicated by red arrows in Figure S9B) to reach the relatively conserved basic residue at position 43, which should be ideally suited to bind to the PPant phosphate group in the catalytically competent complex based on distance considerations. Whereas ACP in the initial encounter complex mainly interacts with basic residues located on helix $\alpha 2$ (Figure S9A), the closure of the SBL might enable ACP to move closer to the newly created positively charged amino acid patch surrounding this loop (Figures S9B and S9C). We note that the essential dynamics observed for the SBL and helix $\alpha 2$ might be directly involved in this substrate recognition process.

As for β -ketoacyl ACP synthases of the FAS-II pathway^{18, 19}, induced-fit effects seem to play a pivotal role during the binding process of ACP-bound substrates. We propose that binding of the reduced cofactor to the ecFabI-ACP encounter complex (according to our new interpretation of the structure with the PDB code 2FHS, which was obtained based on a crystallization trial in the presence of the oxidized cofactor)¹⁷ will initiate the formation of the catalytically competent complex via the concerted closure of the SBL and injection of the substrate to the FabI binding-site (Figure S9B). The highly conserved ACP residue Ile54, which displayed the largest chemical shift perturbation in NMR experiments with FabG and ACP¹⁶, contacts the acyl-substrate within the ACP-fold and is located close to the SBL in the FabI-ACP complex indicating that this residue might be involved in this concerted process (Figure S9C). In FabI, the conserved basic residue at position 194 (193 for ecFabI, see also Figure S9A) might also be crucial for this process since it can interact electrostatically with the ACP and was suggested to function as a hinge for SBL closure together with a hydrogen bond acceptor at position 205²⁰.

An important question concerning the binding of the substrate is whether FabI recognizes its correct interaction partner based on slightly varying ACP conformations for different FAS-II intermediates or just after injection of each substrate¹⁶. During our kinetic experiments, we found that the octenoyl-CoA substrate and its saturated octanoyl-CoA product bind with similar affinity to the enzyme (estimated K_d , octenoyl-CoA = 100 μ M¹², K_i , octanoyl-CoA = 96 \pm 21 μ M). The inability of saFabI to differentiate these two CoA-species indicates that substrate recognition has to occur

at the ACP level prior to substrate delivery, which is much more efficient than scanning all substrates inside the binding pocket.

Supplemental References

1. Weiss, M. (2001) Global indicators of X-ray data quality, *Journal of Applied Crystallography* 34, 130-135.
2. Davis, I. W., Leaver-Fay, A., Chen, V. B., Block, J. N., Kapral, G. J., Wang, X., Murray, L. W., Arendall, W. B., 3rd, Snoeyink, J., Richardson, J. S., and Richardson, D. C. (2007) MolProbity: all-atom contacts and structure validation for proteins and nucleic acids, *Nucleic Acids Res* 35, W375-383.
3. Theobald, D. L., and Steindel, P. A. (2012) Optimal simultaneous superpositioning of multiple structures with missing data, *Bioinformatics* 28, 1972-1979.
4. (1994) The CCP4 suite: programs for protein crystallography, *Acta Crystallogr D Biol Crystallogr* 50, 760-763.
5. R Development Core Team. (2010) R: A language and environment for statistical computing, R Foundation for Statistical Computing, Vienna, Austria.
6. Mongan, J. (2004) Interactive essential dynamics, *J Comput Aided Mol Des* 18, 433-436.
7. Schiebel, J., Chang, A., Lu, H., Baxter, M. V., Tonge, P. J., and Kisker, C. (2012) *Staphylococcus aureus* FabI: inhibition, substrate recognition, and potential implications for *in vivo* essentiality, *Structure* 20, 802-813.
8. White, S. W., Zheng, J., Zhang, Y. M., and Rock. (2005) The structural biology of type II fatty acid biosynthesis, *Annu. Rev. Biochem.* 74, 791-831.
9. Tanaka, N., Nonaka, T., Tanabe, T., Yoshimoto, T., Tsuru, D., and Mitsui, Y. (1996) Crystal structures of the binary and ternary complexes of 7 alpha-hydroxysteroid dehydrogenase from *Escherichia coli*, *Biochemistry* 35, 7715-7730.
10. Schiebel, J., Chang, A., Shah, S., Lu, Y., Liu, L., Pan, P., Hirschbeck, M. W., Tareilus, M., Eltschkner, S., Yu, W., Cummings, J. E., Knudson, S. E., Bommineni, G. R., Walker, S. G., Slayden, R. A., Sotriffer, C. A., Tonge, P. J., and Kisker, C. (2014) Rational Design of Broad Spectrum Antibacterial Activity Based on a Clinically Relevant Enoyl-Acyl Carrier Protein (ACP) Reductase Inhibitor, *J Biol Chem* 289, 15987-16005.
11. Bell, A. F., Stratton, C. F., Zhang, X., Novichenok, P., Jaye, A. A., Nair, P. A., Parikh, S., Rawat, R., and Tonge, P. J. (2007) Evidence from Raman spectroscopy that InhA, the mycobacterial enoyl reductase, modulates the conformation of the NADH cofactor to promote catalysis, *J Am Chem Soc* 129, 6425-6431.
12. Chang, A., Schiebel, J., Yu, W., Bommineni, G. R., Pan, P., Baxter, M. V., Khanna, A., Sotriffer, C. A., Kisker, C., and Tonge, P. J. (2013) Rational optimization of drug-target residence time: insights from inhibitor binding to the *Staphylococcus aureus* FabI enzyme-product complex, *Biochemistry* 52, 4217-4228.
13. Pan, A. C., Borhani, D. W., Dror, R. O., and Shaw, D. E. (2013) Molecular determinants of drug-receptor binding kinetics, *Drug Discov Today* 18, 667-673.
14. Schmidtke, P., Luque, F. J., Murray, J. B., and Barril, X. (2011) Shielded hydrogen bonds as structural determinants of binding kinetics: application in drug design, *J Am Chem Soc* 133, 18903-18910.
15. Bissantz, C., Kuhn, B., and Stahl, M. (2010) A medicinal chemist's guide to molecular interactions, *J. Med. Chem.* 53, 5061-5084.
16. Zhang, Y. M., Wu, B., Zheng, J., and Rock, C. O. (2003) Key residues responsible for acyl carrier protein and beta-ketoacyl-acyl carrier protein reductase (FabG) interaction, *J Biol Chem* 278, 52935-52943.
17. Rafi, S., Novichenok, P., Kolappan, S., Zhang, X., Stratton, C. F., Rawat, R., Kisker, C., Simmerling, C., and Tonge, P. J. (2006) Structure of acyl carrier protein bound to FabI, the FASII enoyl reductase from *Escherichia coli*, *J Biol Chem* 281, 39285-39293.

18. Schiebel, J., Kapilashrami, K., Fekete, A., Bommineni, G. R., Schaefer, C. M., Mueller, M. J., Tonge, P. J., and Kisker, C. (2013) Structural Basis for the Recognition of Mycolic Acid Precursors by KasA, a Condensing Enzyme and Drug Target from Mycobacterium Tuberculosis, *J Biol Chem* 288, 34190-34204.
19. Borgaro, J. G., Chang, A., Machutta, C. A., Zhang, X., and Tonge, P. J. (2011) Substrate recognition by beta-ketoacyl-ACP synthases, *Biochemistry* 50, 10678-10686.
20. Maity, K., Banerjee, T., Prabakaran, N., Surolia, N., Surolia, A., and Suguna, K. (2011) Effect of substrate binding loop mutations on the structure, kinetics, and inhibition of enoyl acyl carrier protein reductase from plasmodium falciparum, *IUBMB Life* 63, 30-41.